separations

MDPI

Article

Effect of Iron–Carbon–Zeolite Substrate Configuration on Cadmium Removal in Vertical-Flow Constructed Wetlands

Mengyi Li [1,2], Shiyu Chen [3], Jundan Chen [3], Naifu Zhou [4,*] and Guanlong Yu [3]

[1] College of Art and Design, Hunan City University, Yiyang 413000, China; lmyyy2516@163.com
[2] Anhui Hongsen High Technology Forestry Co., Ltd., Bozhou 236000, China
[3] School of Hydraulic Engineering, Changsha University of Science & Technology, Changsha 410114, China
[4] Hunan Provincial Cooperative Center of Water Resources Research and Development, Changsha 410031, China
* Correspondence: zhounaifu1026@163.com; Tel.: +86-731-8898-8706; Fax: +86-731-8898-8706

Abstract

The excessive emission of cadmium (Cd^{2+}) poses a serious threat to the aquatic environment due to its high toxicity and bioaccumulation potential. This study constructed three types of vertical-subsurface-flow constructed wetlands configured with iron–carbon–zeolite composite substrates, including an iron–carbon–zeolite constructed wetland (TF-CW), a zeolite–iron–carbon constructed wetland (FT-CW), and an iron–carbon–zeolite mixed constructed wetland (H-CW), to investigate the purification performance and mechanisms of constructed wetlands for cadmium-containing wastewater (0~6 mg/L). The results demonstrated that iron–carbon–zeolite composite substrates significantly enhanced Cd^{2+} removal efficiency (>99%) through synergistic redox-adsorption mechanisms, where the iron–carbon substrate layer dominated Fe-Cd co-precipitation, while the zeolite layer achieved short-term cadmium retention through ion-exchange adsorption. FT-CW exhibited superior NH_4^+-N removal efficiency (77.66%~92.23%) compared with TF-CW (71.45%~88.05%), while iron–carbon micro-electrolysis effectively inhibited NO_3^--N accumulation (<0.1 mg/L). Under cadmium stress, *Typha* primarily accumulated cadmium through its root systems (>85%) and alleviated oxidative damage by dynamically regulating antioxidative enzyme activity, with the superoxide dismutase (SOD) peak occurring at 3 mg/L Cd^{2+} treatment. Microbial community analysis revealed that iron–carbon substrates promoted the relative abundance of *Bacteroidota* and *Patescibacteria* as well as the enrichment of *Saccharimonadales*, *Thauera*, and *Rhodocyclaceae* (genera), enhancing system stability. This study confirms that iron–carbon–zeolite CWs provide an efficient and sustainable technological pathway for heavy metal-contaminated water remediation through multidimensional mechanisms of "chemical immobilization–plant enrichment–microbial metabolism".

Keywords: constructed wetland; heavy metal; iron–carbon micro-electrolysis; plants; microbial community

check for updates

Academic Editor: John V. Headley

Received: 15 July 2025
Revised: 14 August 2025
Accepted: 17 August 2025
Published: 21 August 2025

Citation: Li, M.; Chen, S.; Chen, J.; Zhou, N.; Yu, G. Effect of Iron–Carbon–Zeolite Substrate Configuration on Cadmium Removal in Vertical-Flow Constructed Wetlands. *Separations* **2025**, *12*, 223. https://doi.org/10.3390/separations12080223

Copyright: © 2025 by the authors. Licensee MDPI, Basel, Switzerland. This article is an open access article distributed under the terms and conditions of the Creative Commons Attribution (CC BY) license (https://creativecommons.org/licenses/by/4.0/).

1. Introduction

With the improper treatment and direct discharge of wastewater and exhaust gases containing substantial quantities of heavy metals (HMs) from industrial processes such as mining, smelting, and chemical production, heavy metal contamination in the environment has become increasingly severe. Cadmium (Cd), as a highly toxic heavy metal, poses serious threats to aquatic ecosystems and human health due to its bioaccumulation potential and persistent nature [1]. Under cadmium stress, plant physiological processes suffer

multiple disruptions, including delayed seed germination, chlorosis symptoms in leaves, and plant wilting with reduced dry matter accumulation [2]. The health hazards are primarily manifested as multi-system damage under chronic exposure, exemplified by the "Itai-itai disease" that occurred in Toyama Prefecture, Japan, where residents who consumed cadmium-contaminated rice over extended periods experienced significant bone density reduction, elevated pathological fracture risks, and pain symptoms persisting for decades [3].

Currently, the primary treatment methods for heavy metal wastewater include chemical, physical, and biological approaches, encompassing chemical precipitation, electrolysis, ion exchange, membrane separation, activated carbon and silica gel adsorption, bioflocculation, and phytoremediation. Constructed wetlands (CWs) have emerged as an important technology for heavy metal wastewater treatment due to their advantages of low cost and sustainability, removing heavy metals through multiple pathways including substrate adsorption, plant uptake, microbial action, and chemical precipitation. Research demonstrates that constructed wetlands can achieve removal efficiencies exceeding 90% for various heavy metals such as copper, zinc, lead, cadmium, and chromium, with some heavy metal removal rates reaching above 95%. However, traditional substrates exhibit insufficient removal efficiency and stability for Cd [4,5]. Li et al. discovered that the combination of biochar and artificial humic acid significantly enhanced cadmium immobilization efficiency through microbially induced calcium carbonate precipitation (MICP) technology while simultaneously improving soil fertility [6]. Wang et al. found that zeolite-modified substrates loaded with Fe_2O_3 nanoparticles and CaO nanoparticles promoted Cu and Ni removal by increasing electrostatic adsorption, chemical precipitation, and the abundance of resistant microorganisms and functional genes [7]. Wang et al. discovered that biochar preferentially adsorbed bioavailable Cd^{2+} in water bodies and significantly increased Fe/Mn oxide-bound and exchangeable Cd fractions [8].

However, how iron–carbon–zeolite composite substrates influence the physicochemical parameters and individual components of constructed wetlands, ultimately enhancing hazardous substance removal efficiency, remains incompletely understood. This study designates Cd^{2+} as the target pollutant and innovatively combines iron–carbon microelectrolytic materials with zeolite to investigate the removal efficiency of constructed wetland systems under different substrate configurations when subjected to increasing Cd^{2+} pollution loads. The study examines the mechanisms of cadmium removal by constructed wetlands and determines the potential effects of plant physiological responses and functional microbial community structures, revealing the synergistic mechanisms of plant–microorganism–substrate interactions. This research holds significant importance for optimizing substrate configurations and reducing plant toxic effects under cadmium stress.

2. Materials and Methods

2.1. Experimental Design

The experiment employed vertical-subsurface-flow constructed wetland (VSSFCW) models with a total height of 60 cm (effective working zone = 55 cm) and a 20 cm diameter, fabricated from polyvinyl chloride (PVC) materials (Figure 1). The substrate structure consisted of three layers: the bottom layer comprised a 15 cm thick gravel support layer with particle sizes of 30–50 mm; the middle layer was a 30 cm thick functional substrate layer (particle size 8–12 mm), divided into three groups according to configuration: FT-CW consisted of an upper 15 cm zeolite layer and a lower 15 cm iron–carbon layer; TF-CW consisted of an upper 15 cm iron–carbon layer and a lower 15 cm zeolite layer; H-CW consisted of iron–carbon and zeolite mixed at a 1:1 volume ratio with a total thickness of 30 cm. The top layer was a 10 cm thick gravel layer with particle sizes of 10–20 mm. All

three systems had an effective water treatment capacity of 7 L, with porosities of 48.6%, 48.3%, and 48.2%, respectively, and a hydraulic load rate of 0.11 $m^3/(m^2 \cdot d)$. *Typha* was selected as the wetland plant, with three seedlings of similar height and good nutritional status transplanted into each system.

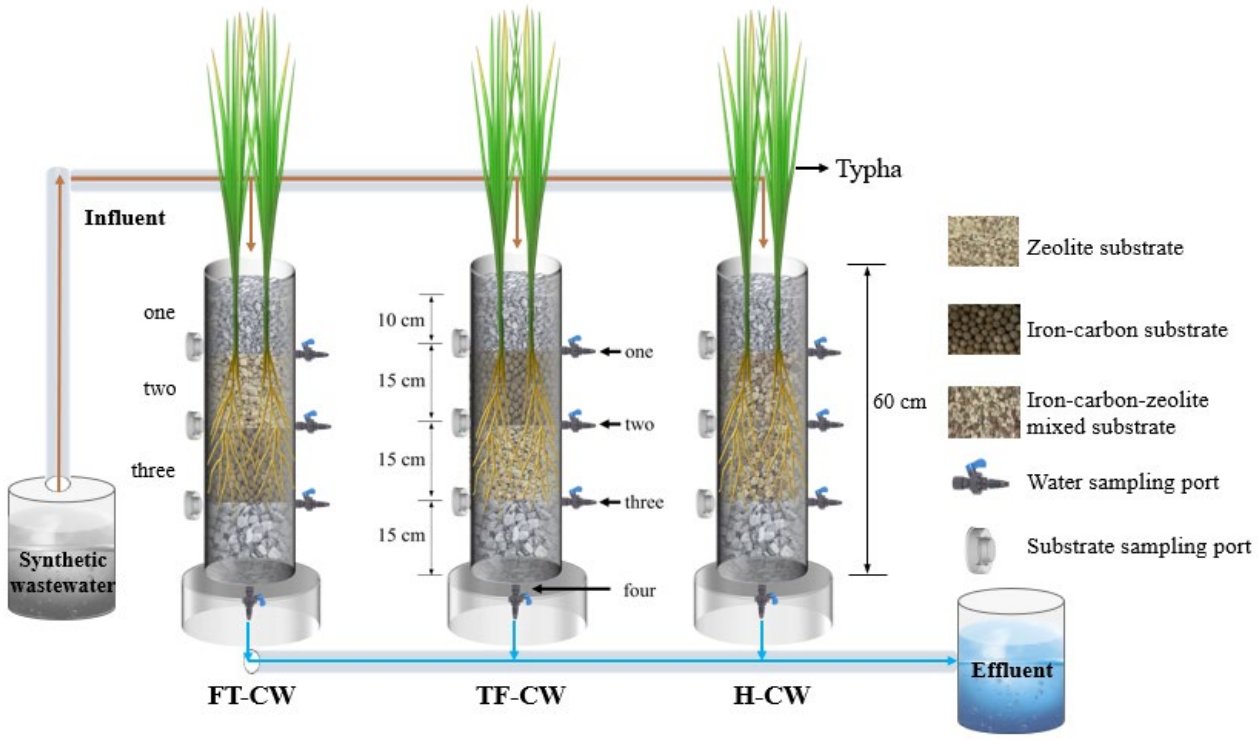


Figure 1. Schematic diagram of the VFCWs (FT-CW, TF-CW, and H-CW).

2.2. Operation of Constructed Wetland Systems

The entire experiment was conducted at the Hydraulic Engineering Experimental Center of Changsha University of Science and Technology (28°06′76″ N, 113°00′43″ E), which is characterized by a subtropical monsoon climate with year-round humidity maintained between 70% and 80%. All the CW systems employed downflow intermittent feeding, with the hydraulic retention time (HRT) set at 2 days. Artificially prepared synthetic wastewater was used as the influent source, with specific water-quality parameters presented in Table 1.

Table 1. Parameters of influent water quality at different stages.

Stage	Influent Concentration (mg/L)				pH	DO (mg/L)	EC [a] (μs/cm)	Duration (d)
	COD	NH_4^+-N	TP	Cd^{2+}				
I	60	40	1	0	7.65 ± 0.20	4.46 ± 0.18	458.07 ± 24.98	36–66
II	60	40	1	3	7.53 ± 0.10	4.46 ± 0.21	363.14 ± 33.50	96–124
III	60	40	1	6	7.60 ± 0.07	4.57 ± 0.20	355.80 ± 22.18	124–153

[a] EC represents the electrical conductivity.

2.3. Sample Collection and Analysis

2.3.1. Water Sample Collection and Detection

In this experiment, iron–carbon–zeolite CW systems with different configurations were constructed. After the systems were constructed, they were first operated continuously for one week to check the tightness of the devices (for leaks). After 36 days of operation, all wetland systems reached a stable state. Water samples were collected from sampling points at outlets one, two, and three as effluent sampling locations, with routine water sample collection and measurements conducted every 2 days. Each sampling involved

taking three parallel water samples at the outlet, and the test results were averaged and the standard deviation calculated. Dissolved oxygen and water temperature were measured using a dissolved oxygen meter (JPBJ-607A; Shanghai Leici Instrument Factory, Shanghai, China), and pH values were detected using a pH meter (pH-100B; Lichen, Shanghai, China). All water samples were filtered through 0.45 μm water-quality injection filters, and Cd^{2+} concentrations were subsequently measured using atomic absorption spectrophotometry (AA6800; Shimadzu Co., Kyoto Japan).

2.3.2. Plant Sampling and Analysis

Based on established extraction methods with modifications, the photosynthetic pigment, superoxide dismutase (SOD), malondialdehyde (MDA), and hydrogen peroxide (H_2O_2) content in plant leaves was determined at the end of each experimental stage, with detection performed using ultraviolet spectrophotometry. Specific determination procedures and calculations for the plant analysis indicators are presented in Table 2.

Table 2. Plant physiological indicators and analytical methods.

Analysis Parameter	Analysis Item	Detection Wavelength (nm)	Calculation Formula	Review
Photosynthetic Pigments	Chl [2] a, Chl b, The total amounts of carotenoids	470, 649, 665	$C_a = 13.95A_{665} - 6.88A_{649}$ $C_b = 24.96A_{649} - 7.32A_{665}$ $C_{x+c} = (1000A_{470}2.05C_a \times 114.8C_b)/245$	[9]
ROS [1]	H_2O_2	390	/	[10]
Lipid Peroxidation	MDA [3]	532, 600, 450	C [5] $= 6.45\,(A_{532} - A_{600}) - 0.56A_{450}$	[11]
Antioxidative Enzymes	SOD [4]	560	C [6] $= (A_{ck} - A_c) \times V/(50\% \times A_{ck} \times W \times Vt)$	[12]

[1] Reactive oxygen species; [2] Chlorophyll; [3] Malondialdehyde; [4] Superoxide dismutase; C_a: Chlorophyll a concentration (mg/L); C_b: Chlorophyll b concentration (mg/L); C_{x+c}: The total amounts of carotenoid concentration (mg/L); C [5]: MDA concentration (μmol/L); C [6]: SOD concentration (U/g FW); A_{ck}: Absorbance of the light control tube; A_c: Absorbance of sample tubes; V: Total volume of sample liquid; W: Fresh weight of sample (g); Vt: Enzyme solution volume used during measurement (mL, 30 μL).

Upon completion of the entire experiment, both aboveground and belowground plant parts were washed with tap water and distilled water, and the mass of each part was weighed. Cadmium extraction from plant tissues was performed using concentrated HNO_3 microwave digestion, and cadmium concentrations were detected using atomic absorption spectrophotometry (AA6800; Shimadzu, Japan) according to standard methods. Detailed procedures for the plant analysis are provided in Table 2.

2.3.3. Substrate Sample Collection and Analysis

At the end of each stage, substrate samples were collected based on established methods [13] for cadmium speciation analysis using sequential extraction procedures and extracellular polymeric substance (EPS) analysis. Cadmium species in the substrates were classified into five operationally defined fractions based on the modified Tessier sequential extraction procedure: exchangeable fraction (EXC), carbonate-bound fraction (CAR), iron–manganese-bound fraction (Fe-Mn), organically bound fraction (ORG), and residual fraction (RES). This classification scheme allows for the assessment of cadmium mobility and bioavailability, with the exchangeable fraction representing the most labile and bioavailable form, while the residual fraction represents the most stable and least bioavailable form. Different cadmium species were analyzed using atomic absorption spectrophotometry (AA6800; Shimadzu, Japan), and protein content was determined using the Folin phenol reagent method.

2.3.4. Microbial Sample Collection and Analysis

Upon completion of Stage III experiments, representative substrate samples were collected from each layer using duplicate centrifuge tubes and submitted to Shanghai Meiji Biomedical Technology Co., Ltd. (Shanghai, China) for microbial community analysis.

DNA purity and concentration were determined using NanoDrop2000, and integrity was assessed by 1.0% agarose gel electrophoresis. The bacterial V3-V4 hypervariable region of 16S rRNA was amplified using primers 335F (ACTCCTACGGGAGGCAGCAG) and 806R (GGACTACHVGGGTWTCTAAT). PCR products were precisely quantified using the QuantiFluor™-ST blue fluorescence quantification system (Promega Corporation, Madison, WI, USA). Sequencing libraries were constructed using the TruSeq™ DNA Sample Prep Kit (Illumina, Shenzhen, China), and sequencing was performed on the Illumina MiSeq PE300 platform (Illumina, Shenzhen, China). Subsequent microbial-related analyses were completed using the Majorbio Cloud Platform (Shanghai Meiji Biomedical Technology Co., Ltd., Shanghai, China).

3. Results and Discussion

3.1. Effects of Cadmium on the Pollutant Removal Performance of Iron–Carbon–Zeolite Constructed Wetlands

3.1.1. Cd^{2+} Removal Efficiency and Mechanisms

Cadmium removal in constructed wetlands is primarily achieved through synergistic mechanisms, including plant uptake and accumulation, substrate adsorption and precipitation, and microbial action [14]. Figure 2 shows the changes in DO, EC, and pH concentrations at the outlet of the fourth layer of the iron–carbon–zeolite constructed wetland under different Cd^{2+} concentrations in the influent. Figure 3 shows the Cd^{2+} concentration variations at different outlet points and corresponding removal efficiencies for constructed wetlands with different configurations across the various experimental stages. As shown in Figure 3a, immediately after cadmium addition to the influent in Stage II, FT-CW and TF-CW exhibited relatively low cadmium removal rates, with significant fluctuations in effluent cadmium concentrations showing a gradual upward trend. As the reaction continued, removal efficiency gradually increased until stabilization. This phenomenon occurs because plants and microorganisms in the wetland systems require an adaptation period to the introduced cadmium stress during the initial experimental stage [15]. At this time, the microbial community structure may not yet have been adjusted, with insufficient quantities or inhibited activity of specific cadmium-tolerant microorganisms, resulting in limited efficiency toward cadmium decomposition or immobilization. As the reaction progresses under continuous cadmium exposure pressure, microbial communities in the wetland systems undergo succession, with cadmium-tolerant microorganisms gradually becoming dominant populations [16]. By Stage III, cadmium removal efficiencies for FT-CW and TF-CW had improved from 81.61% and 95.29% to 91.29% and 96.56%, respectively.

Iron–carbon–zeolite composite constructed wetlands demonstrated significant Cd^{2+} removal efficiency. The removal efficiencies of the three configurations (FT-CW, TF-CW, and H-CW) at the fourth outlet in Stage III (Cd^{2+} concentration of 6 mg/L) were 99.713% $\pm$ 0.292%, 99.568% $\pm$ 0.402%, and 99.659% $\pm$ 0.309%, respectively (Figure 3c). Vertical analysis revealed that Cd^{2+} removal exhibited gradient characteristics: in the third substrate layer, FT-CW's cadmium removal efficiency improved by 17.92% $\pm$ 7.22% and 8.12% $\pm$ 1.55% compared with the second layer, while TF-CW showed improvements of 4.23% $\pm$ 2.68% and 2.85% $\pm$ 1.77%, indicating that the iron–carbon composite substrates located in the deeper zones (outlets 3) demonstrate significantly superior cadmium immobilization capacity compared with the zeolite substrates predominantly present at outlet 2 (Figure 3b). This enhanced performance can be attributed to multiple synergistic mechanisms: The iron–carbon substrates create micro-galvanic cells whereby iron acts as an electron donor, generating Fe^{2+} ions that subsequently oxidize to Fe^{3+}, forming iron hydroxides and oxyhydroxides with high affinity for cadmium adsorption and co-precipitation [17]. The iron–carbon composite possesses a more complex porous structure

and higher specific surface area compared with zeolite, providing more active sites for cadmium binding through surface complexation and electrostatic interactions [18]. Specifically, FT-CW and TF-CW achieved average Cd^{2+} removal rates of 91.29% ± 2.02% and 95.56% at the second outlet during Stage III, representing increases of 9.68% and 5.27%, respectively, compared with Stage II (Figure 3b). In Stages II and III, the removal efficiency of cadmium by the three devices exceeded 99%.

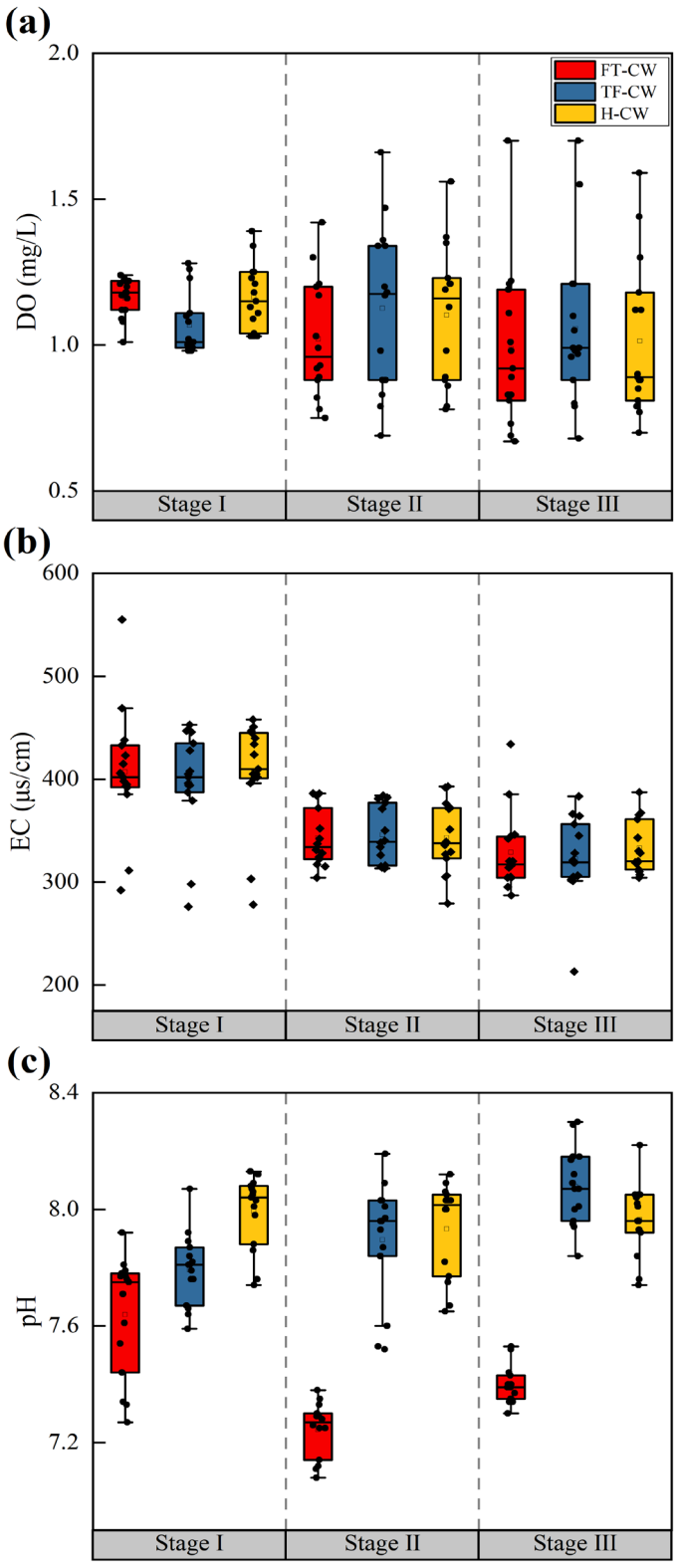


Figure 2. Vertical variation curves of effluent DO (**a**), EC (**b**), and pH (**c**) for each operational stage.

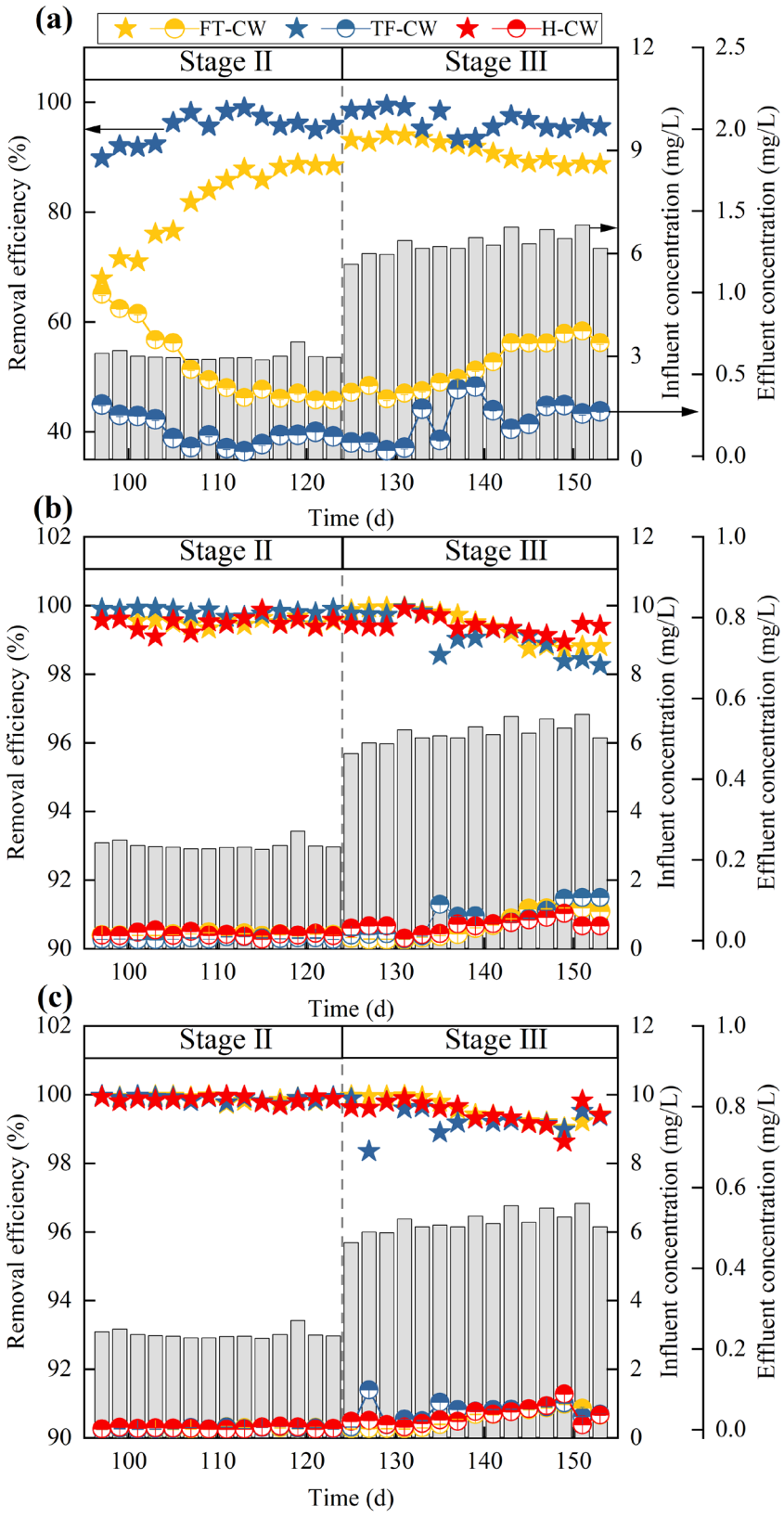


Figure 3. Variation of effluent Cd^{2+} concentration and its removal rate at two (**a**), three (**b**), and four (**c**) outlets under different influent Cd^{2+} concentrations. Values represent the mean of three replicates across four experiments, and error bars represent the standard deviation (n = 3).

Figure 4 shows the accumulation distribution of different cadmium compounds in the second and third layers of the iron–carbon–zeolite matrix in the second and third stages.

Redox mechanisms in iron-carbon layers: Fe^{2+} is oxidized to Fe^{3+}, which is hydrolyzed to form iron oxides/hydroxides (such as FeOOH and $Fe(OH)_3$) and fixed with Cd^{2+} through surface complexation and coprecipitation to form stable Cd-Fe complexes [19]. All CW effluents maintained weak alkalinity (pH 7.4–8.1). Within this range, Fe^{2+} released from the Fe/C microelectrolysis anode was rapidly oxidized to Fe^{3+} and coprecipitated with trace amounts of Mn^{2+}/Mn^{4+} in the iron filings to form amorphous iron–manganese (oxyhydroxide) oxide. Active hydrogen ([H]) reduces part of the Cd^{2+} to low-mobility Cd^0. As shown in Figure 2a–c, the effluent pH from all three CW systems remained weakly alkaline across all stages, with TF-CW consistently exhibiting higher pH values than FT-CW at different outlets across the stages, further confirming TF-CW's superior cadmium removal performance compared with that of FT-CW. Meanwhile, the zeolite layer relies on cation exchange (such as Ca^{2+}/Cd^{2+} replacement) and carbonate-bound adsorption, demonstrating high short-term adsorption efficiency but presenting risks of secondary release [20,21]. The bioavailability of cadmium is significantly reduced through several interconnected processes: The iron–carbon micro-electrolysis process transforms dissolved Cd^{2+} into less mobile forms, such as the iron–manganese-bound fraction, the residual fraction, and the carbonate-bound fraction [22]. The combination of iron–carbon and zeolite creates heterogeneous interfaces with enhanced adsorption properties due to the formation of composite binding sites with higher affinity for cadmium [17]. Substrate layers containing iron–carbon materials (TF-CW and FT-CW systems) displayed markedly elevated levels of iron–manganese oxide-associated fractions compared with alternative substrate configurations during Stages II–III. In Stage III, bound cadmium accumulation in the iron–carbon layer reached 128.87 mg/kg, while exchangeable cadmium content in the zeolite layer ranged from 7.91 to 12.70 mg/kg, validating the dominant role of iron–carbon layers in long-term immobilization (Figure 4c,d).

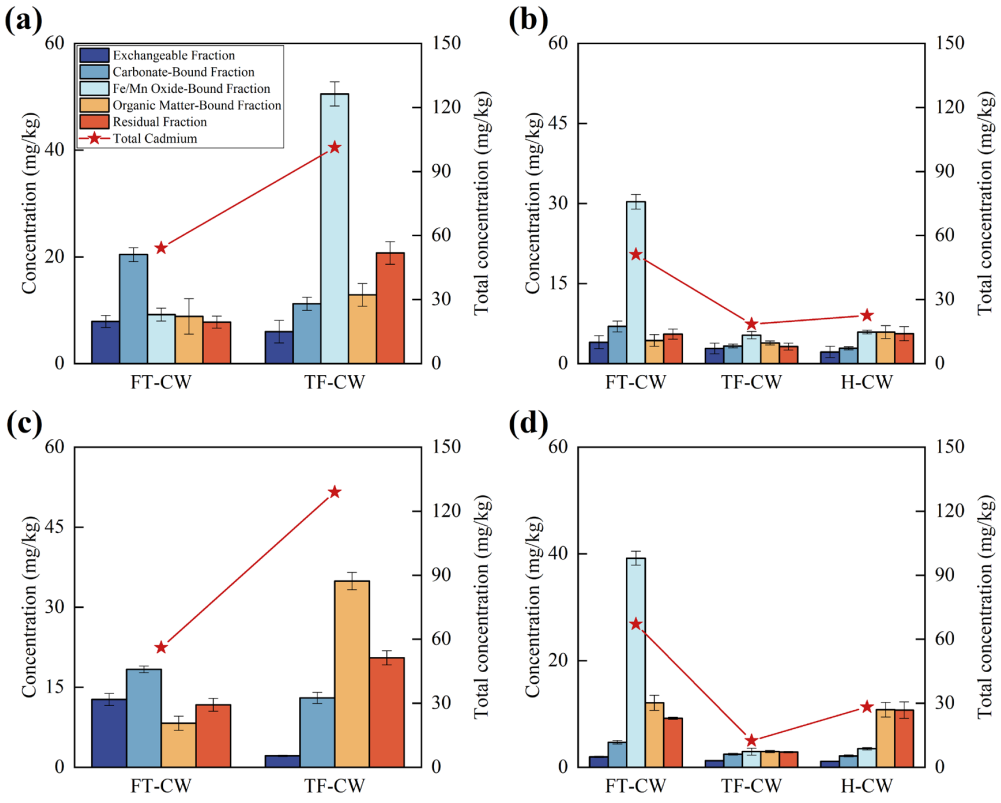


Figure 4. Accumulation of different cadmium species in layers two and three of iron–carbon–zeolite substrates during Stage II (**a**,**b**) and Stage III (**c**,**d**).

3.1.2. NH_4^+-N Removal

Figure 5a–c illustrates the effluent NH_4^+-N concentration variations and corresponding removal-efficiency patterns at different sampling points along the flow path of iron–carbon–zeolite composite constructed wetland systems under three influent cadmium concentration gradients (0, 3, and 6 mg/L, respectively) across different experimental stages (Figure 5a–c).

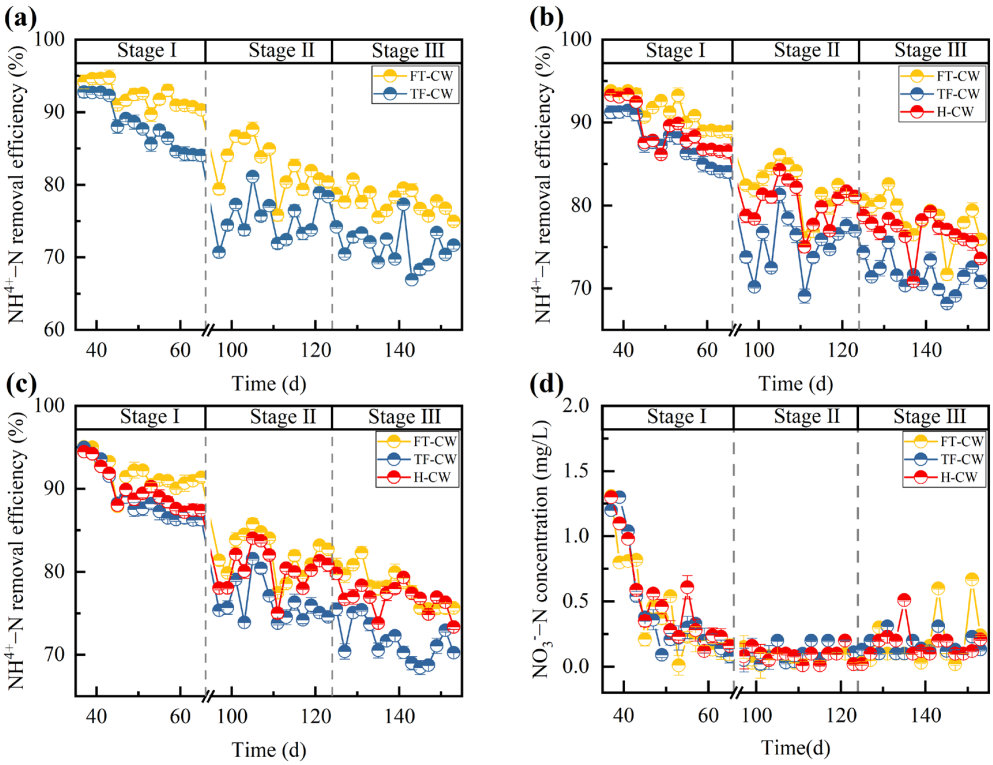


Figure 5. Variation of the NH_4^+-N removal rate at different stages at two, three, and four outlets (**a**–**c**); NO_3^--N effluent concentration at the fourth outlet (**d**). Values represent the mean of three replicates across four experiments, and error bars represent the standard deviation (n = 3).

FT-CW (zeolite upper-layer configuration) achieved the highest NH_4^+-N removal efficiency across the three stages (from 92.23% in Stage I to 77.66% in Stage III, with a decline of 14.57%), significantly outperforming TF-CW (from 88.05% in Stage I to 71.45% in Stage III, with a decline of 16.6%) and H-CW (from 89.79% in Stage I to 76.87% in Stage III, with a decline of 12.4%) (Figure 5a). Vertical data analysis revealed that as the influent Cd^{2+} concentration increased, NH_4^+-N removal efficiency in the CWs gradually decreased. However, across Stages I, II, and III, the differences in effluent NH_4^+-N removal rates between different layers remained below 1.1%, indicating relatively uniform dissolved oxygen distribution within the systems, with aerobic nitrification being the dominant process (Figure 2a). The zeolite upper layer in FT-CW promoted atmospheric reaeration and plant oxygen release through its porous structure, providing a high-DO microenvironment for ammonia-oxidizing bacteria (AOB) [23]; whereas the iron–carbon layer in TF-CW consumed substantial DO through micro-electrolytic reactions, creating oxygen competition with nitrifying bacteria and inhibiting the NH_4^+-N conversion efficiency [24,25].

3.1.3. Nitrate Nitrogen Accumulation

Figure 5d illustrates the dynamic variation characteristics of NO_3^--N concentrations in terminal effluent under different Cd^{2+}-loading conditions across various CW configurations. The experimental data demonstrated that as the operational time extended, NO_3^--N

concentrations at the fourth outlet remained stable at below 0.1 mg/L, with no significant accumulation observed (Figure 5d).

This phenomenon can be explained by the multiple mechanisms of iron–carbon micro-electrolysis: zero-valent iron (Fe^0) directly reduces NO_3^--N as an electron donor; active hydrogen ([H]) and Fe^{2+} generated from micro-electrolysis provides electron sources for autotrophic denitrifying bacteria (such as *Thauera* and *Rhodocyclaceae*), accelerating the NO_3^--N conversion to N_2 [26].

$$4Fe^0 + NO_3^- + 10H^+ \rightarrow 4Fe^{2+} + NH_4^+ + 3H_2O$$

Additionally, the porous structure of activated carbon adsorbs organic matter, providing carbon sources for heterotrophic denitrification, while iron corrosion products (such as $Fe(OH)_3$) further enhance nitrate removal through flocculation and precipitation [27,28]. These synergistic effects enabled the system to maintain efficient denitrification performance; therefore, even under varying Cd^{2+} concentration conditions, NO_3^--N did not exhibit obvious accumulation phenomena.

3.2. Effects of Iron–Carbon–Zeolite Constructed Wetlands on the Plant Response Under Cadmium Stress

Cadmium Accumulation and Antioxidant Regulation

Typha root systems exhibited Cd^{2+} accumulation rates exceeding 85%, which were significantly higher than those in stems and leaves (<15%). The experimental data demonstrated that cadmium accumulation in plant roots reached 575.2 mg/kg in the FT-CW system (zeolite–iron–carbon stratified configuration), significantly higher than that in the TF-CW (490.3 mg/kg) and H-CW (476.5 mg/kg) systems (Figure 6). This phenomenon is closely associated with the crucial role of iron in plant heavy metal-tolerance mechanisms. Based on previous studies [24–26], the differential Cd removal efficiency between wetland configurations may be attributed to iron-mediated mechanisms, although direct evidence was not obtained in this study. Literature suggests that iron plaque formation on root surfaces can immobilize Cd through surface coordination [29]. Additionally, iron-mediated redox reactions have been reported to promote root secretion of low-molecular-weight organic acids, which may form stable complexes with Cd^{2+} [30,31]. However, these mechanisms require further investigation through direct measurements of root exudates and iron precipitation dynamics. The positioning of iron–carbon materials in different wetland layers could potentially influence these processes, although quantitative assessment of spatiotemporal iron distribution was beyond the scope of this study. Our findings on Cd speciation changes provide indirect support for these hypothesized mechanisms and highlight the need for future research to directly examine iron–root–Cd interactions in constructed wetlands.

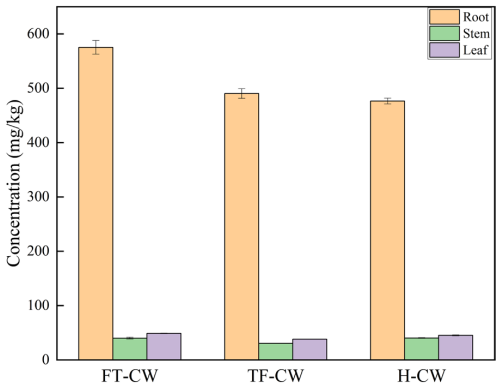


Figure 6. Cadmium accumulation in different parts of the plants at the end of the experiment.

Oxidative stress indicators revealed response differences between the systems. Under cadmium stress, plants alleviated oxidative damage through dynamic regulation of antioxidative enzyme activity; superoxide dismutase (SOD) activity reached its peak during Stage II (3 mg/L Cd^{2+}), subsequently declining as the system adaptability increased (Figure 7d). This pattern reflects plant response strategies to progressive stress: an initial elevation of SOD activity to scavenge excess reactive oxygen species, followed by later-stage (Stage III) reliance on root mucilage barrier formation and microbial resistance evolution [32]. This dual mechanism reduces the Cd^{2+} bioavailability, thereby decreasing antioxidative enzyme requirements. In TF-CW, the front-positioned iron–carbon layer resulted in root exposure to high concentrations of Fe^{2+}, which not only interfered with magnesium ion uptake but may also have induced oxidative stress through Fenton reactions, inhibiting chloroplast function [33]. Its total photosynthetic pigment content (Stage III: 9.70 mg/g) was significantly lower than that in FT-CW (10.58 mg/g) and H-CW (12.03 mg/g) (Figure 7b).

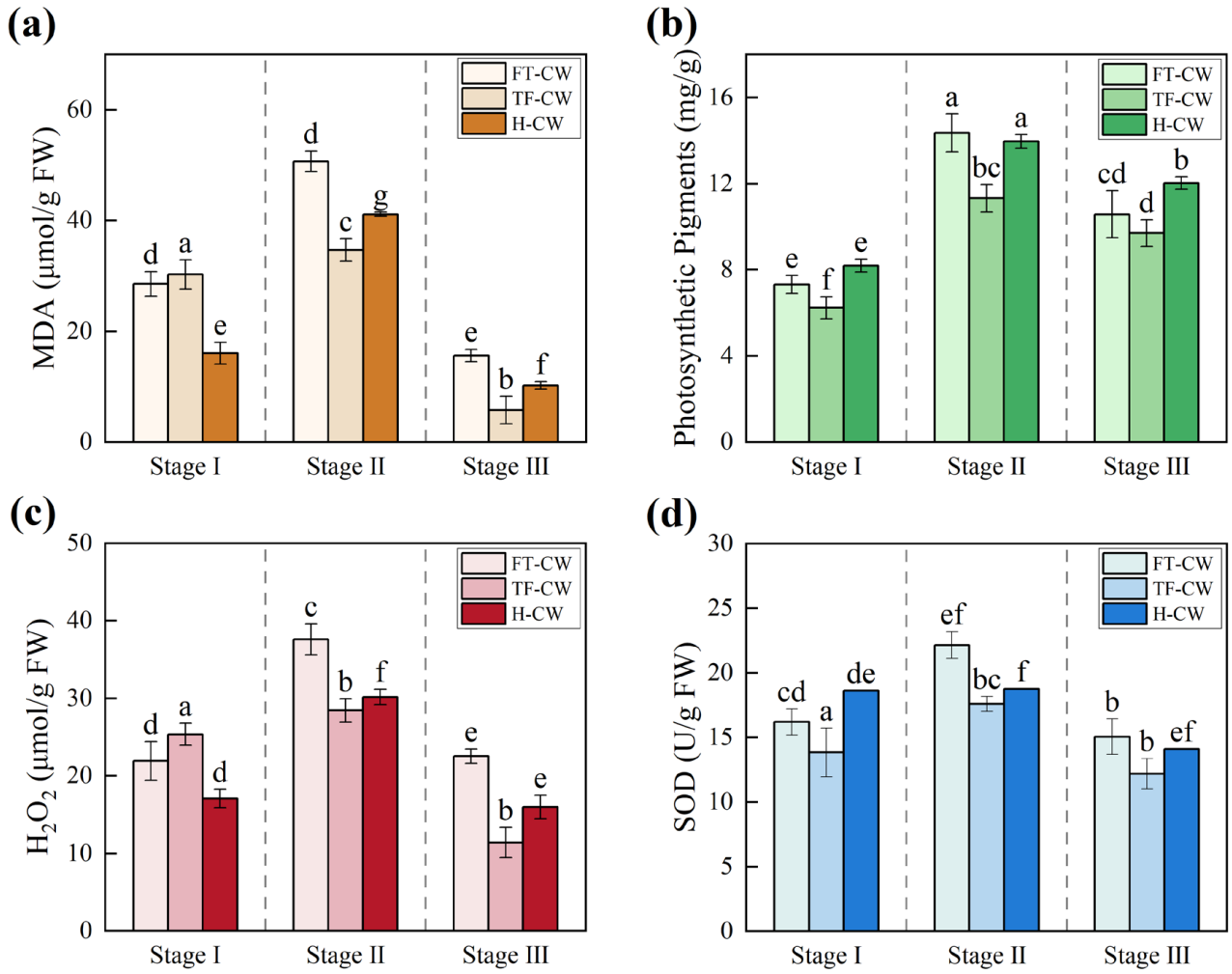


Figure 7. Levels of plant MDA (**a**), photosynthetic pigments (**b**), H_2O_2 (**c**), and SOD (**d**) in iron–carbon–zeolite constructed wetlands under different cadmium concentrations. Different letters indicate significant differences among the four treatments ($p < 0.05$). Values represent the mean of three replicates across four experiments, and error bars represent the standard deviation (n = 3).

The cadmium-induced reactive oxygen species (ROS) burst in Stage II led to dramatic increases in H_2O_2 (reaching 37.62 μmol/g in FT-CW) and the membrane lipid peroxidation product MDA (50.68 μmol/g). However, as the system achieved efficient NH_4^+-N retention (73.8%), root cadmium accumulation decreased, and oxidative damage was significantly

alleviated in Stage III (Figure 7a,c). This indicates that plants mitigate physiological damage by reducing heavy metal translocation to aboveground tissues through selective retention mechanisms. This phenomenon aligns with Jia et al.'s conclusions regarding the influence of heavy metal spatial distribution on physiological metabolism [34].

3.3. Effects of Cadmium on Microorganisms in Iron–Carbon–Zeolite Constructed Wetlands

3.3.1. EPS Secretion and Biofilm Formation

In the wetlands at Stage I (in the absence of cadmium), the FT-CW, TF-CW, and H-CW systems exhibited higher TB-EPS concentrations, which was attributed to the high DO levels (>1.00 mg/L) in the wetland systems during the first stage, indicating that aerobic metabolism was dominant. Under these conditions, microorganisms tend to produce more TB-EPSs to maintain optimal cellular hydration and nutrient retention within the biofilm matrix, consistent with established principles of biofilm physiology [35]. Analysis of the EPS content across different substrate layers under various Cd^{2+} concentration gradients revealed that soluble EPSs (S-EPSs) consistently exhibited low proportions across all stages. As microbial metabolic products, S-EPSs readily dissociate from cell surfaces into the liquid-stage environment, with its accumulation closely related to dissolved oxygen (DO) levels. In this study, effluent DO values in all layers were at around 1.00 mg/L (Figure 2a), indicating that aerobic metabolism dominated within the system, which aligns with Zhou et al.'s findings that S-EPSs accumulate more readily in anaerobic environments (DO < 0.5 mg/L) [36]. Under high DO conditions, enhanced microbial activity leads to rapid S-EPS degradation, thereby limiting its accumulation.

Regarding dynamic responses to cadmium stress, tightly bound EPSs (TB-EPSs) dominated in substrate layers during Stage II, while the proportion of loosely bound EPSs (LB-EPSs) increased significantly in Stage II, with TB-EPSs again becoming the major component by Stage III. This phenomenon reveals adaptive strategies employed by microorganisms to cope with heavy metal stress: when the system was initially exposed to cadmium contamination (Stage II), microorganisms increased LB-EPS secretion to form physical barriers, utilizing their high mass-transfer-resistance characteristics to prevent Cd^{2+} penetration into cells [37]. As the system's cadmium resistance capacity improved (Stage III), the conversion rate from LB-EPSs to TB-EPSs slowed, promoting TB-EPS re-accumulation. This dynamic adjustment mechanism of EPS components helps maintain microbial metabolic homeostasis in cadmium-contaminated environments.

Different substrate combinations exhibited significant differences in EPS distribution characteristics. In the second layer, TF-CW demonstrated EPS contents that were 67.85, 34.23, and 11.80 mg/kg higher than that of FT-CW in Stages I, II, and III, respectively (Figure 7a). The micro-electrolytic action of iron–carbon materials can release Fe^{2+}/Fe^{3+} ions, which reduce the electrostatic repulsion between microbial cells through charge neutralization effects, thereby promoting EPS formation and accumulation [38]. Additionally, TF-CW exhibited lower DO levels in the second layer compared with FT-CW, potentially inhibiting aerobic microbial metabolism and resulting in reduced EPS degradation rates. However, as the Cd^{2+} concentration increased, the differences between the two groups gradually diminished, indicating that microbial dependence on EPS secretion weakened after enhanced system resistance.

In the third layer, FT-CW achieved EPS contents of 114.61 and 48.73 mg/kg in Stages II and III, respectively, which were significantly higher than those of TF-CW (67.97, 28.06 mg/kg) and H-CW (88.64, 38.93 mg/kg) (Figure 8b). This phenomenon may be associated with the dual effects of iron–carbon substrates; reactive species generated from iron–carbon micro-electrolysis promote Cd^{2+} immobilization, reducing toxic pressure

on microorganisms. This aligns with research findings by He et al. [39], where microbial EPS secretion requirements decreased as system heavy metal retention efficiency improved.

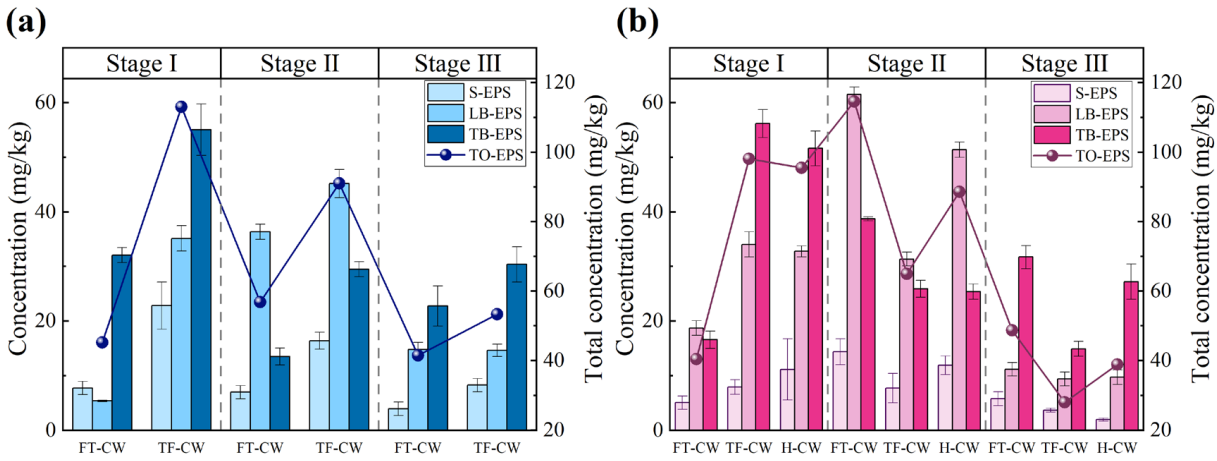


Figure 8. Variation of EPS content in the second (**a**) and third (**b**) layers at each stage of the constructed wetlands.

EPSs demonstrate significant "double-edged sword" effects in pollutant removal processes: it enhances microbial attachment to promote biofilm formation and improve pollutant contact efficiency, but excessive accumulation may cover active sites on cell surfaces, impeding mass transfer and causing substrate clogging [40]. This study found that H-CW maintained relatively high TB-EPS levels (27.20 mg/kg) in Stage III while exhibiting a lower MDA content (10.21 μmol/g FW), indicating that optimized substrate combinations can balance the growth-promoting effects of EPSs with mass-transfer limitations (Figure 8b). For future engineering applications, dynamic management of EPS secretion through the regulation of hydraulic loading or the introduction of functional bacterial communities is recommended to enhance the long-term operational stability of constructed wetland systems.

3.3.2. Microbial Community Structure Analysis

In this study, we conducted a systematic analysis of microbial community characteristics in three constructed wetland systems (FT-CW, TF-CW, H-CW). Table 3 presents the Alpha diversity of microbial communities in iron–carbon–zeolite CWs after the completion of Stage III. Alpha diversity indices revealed that the third layer of the FT-CW system and the second layer of the TF-CW system exhibited the most exceptional community diversity characteristics, specifically manifested as significantly elevated Chao1 and Ace indices, while the Shannon index reached peak values and the Simpson index decreased to minimum levels, indicating that microbial abundance on zeolite substrate surfaces was notably lower than that on iron–carbon composite substrates. In contrast, the H-CW system demonstrated lower values in both the Shannon and Ace indices.

Table 3. Alpha diversity of microbial communities in Stage III iron–carbon–zeolite CWs.

CWs	Substrate Layer	ACE	Chao1	Shannon	Simpson	Coverage
FT-CW	2	678.35	650.08	2.91	0.20	0.998
	3	793.63	791.63	3.51	0.12	0.997
TF-CW	2	875.36	852.69	3.64	0.09	0.997
	3	543.80	538.33	1.92	0.41	0.998
H-CW	3	585.22	576.04	2.68	0.19	0.998

Figure 9 illustrates the microbial composition at phylum and genus levels in various CWs during Stage III. At the phylum level (Figure 9a), *Actinobacteriota*, *Proteobacteria*,

Patescibacteria, *Desulfobacterota*, and *Bacteroidota* were the dominant phyla, accounting for over 90% of the total microbial community. *Bacteroidota* immobilizes heavy metal ions through the secretion of extracellular polymeric substances (EPSs) to form stable complexes, thereby reducing heavy metal mobility and toxicity [8], which aligns with the findings in Section 3.3.1 that the EPS content on iron–carbon substrate surfaces was higher than that on zeolite. *Patescibacteria* participates in pollutant transformation and removal in conjunction with other functional bacterial groups (such as *Proteobacteria*, *Firmicutes*, and *Bacteroidota*) [41]. The relative abundance of *Patescibacteria* on iron–carbon substrate surfaces was significantly higher than in zeolite layers, with *Patescibacteria* proliferation accompanied by decreased *Actinobacteria* abundance. The latter may contain denitrification-inhibiting bacterial groups, whose reduction may facilitate the function of denitrifying bacteria (such as *Nitrospira*). Based on the aforementioned analysis, zeolite demonstrated superior NH_4^+-N removal compared with iron–carbon; therefore, it can be inferred that zeolite's NH_4^+-N removal effectiveness results from ion exchange and adsorption rather than nitrification processes. Furthermore, the relative abundance of *Actinobacteriota* on zeolite substrate surfaces (36.20% and 10.51%) was markedly lower than on iron–carbon substrate surfaces (42.34% and 80.64%). As oligotrophic bacteria, *Actinobacteriota* tends to thrive in environments with limited available carbon sources [42], however, carbon release from iron–carbon substrates provides a relatively abundant carbon supply for microorganisms, and these environmental conditions led to a significantly reduced relative abundance of *Actinobacteriota* in this system.

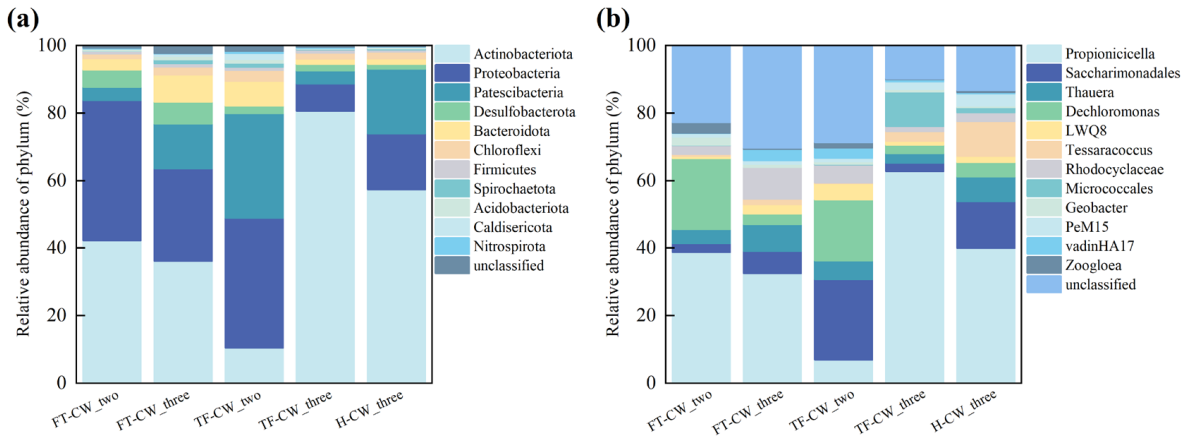


Figure 9. Relative abundance of bacteria in the CWs. Relative abundance of the top 12 phyla and the top 13 genera (including unclassified genera). (**a**) Analysis of microbial composition at the phylum level in Stage III iron-carbon-zeolite constructed wetlands. (**b**) Analysis of microbial genus composition in phase III iron-carbon-zeolite constructed wetlands.

Genus-level analysis revealed that iron–carbon substrates significantly enriched denitrifying bacteria (Thauera, Rhodocyclaceae) and cadmium-tolerant bacteria (Saccharimonadales). For instance, the relative abundance of Thauera and Rhodocyclaceae in the iron–carbon layers of TF-CW and FT-CW reached maximum values of 8.09% and 9.32%, respectively, which were significantly higher than in zeolite layers (with enhancement factors of 2–6 times). Rhodocyclaceae possesses both heterotrophic and hydrogen-autotrophic denitrification capabilities [43], while Thauera is a typical facultative anaerobic denitrifying genus [44]. This phenomenon indicates that the sustained electron-donor effects generated from iron–carbon micro-electrolysis effectively promoted denitrification processes. Some strains within the detected Zoogloea genus are also heterotrophic denitrifying bacteria capable of efficiently removing NO_3^--N using organic carbon sources. Consequently, relatively low NO_3^--N accumulation concentrations were observed in the iron–carbon–zeolite composite

constructed wetland systems. Furthermore, the relative abundance of Saccharimonadales in the iron–carbon layers of TF-CW and FT-CW was 23.76% and 6.57%, respectively, and 13.92% in H-CW, which were markedly higher than in zeolite layers (2.45% and 2.65%), indicating that front-positioned iron–carbon configurations enhanced cadmium-tolerant bacterial enrichment through oxidative environments. Both Saccharimonadales and LWQ8 are classified under Patescibacteria, which aligns with the higher relative abundance of Patescibacteria observed in the phylum-level analysis of iron–carbon layer samples from FT-CW and TF-CW. Additionally, the VadinHA17 genus exhibited similar enrichment trends. As a fermentative bacterium, VadinHA17 can degrade complex organic compounds in wastewater. Research by Pang et al. [45], confirmed that constructed wetland systems containing iron–carbon substrates enhanced the relative abundance of VadinHA17, which is consistent with the results observed in this experiment.

3.4. Substrate Configuration Optimization Analysis

This study compared cadmium accumulation and speciation distribution patterns among three iron–carbon–zeolite constructed wetland substrates (FT-CW, TF-CW, and H-CW) to elucidate their immobilization and transformation mechanisms. Due to the different adsorption substrates, cadmium species in the substrates were classified into exchangeable, carbonate-bound, iron–manganese-bound, organically bound, and residual fractions [46].

As shown in Figure 4, the iron–carbon layers (such as in TF-CW and FT-CW) exhibited significantly higher iron–manganese oxide-bound fractions than other substrate layers throughout Stages II–III, while zeolite layers (such as in FT-CW) relied on cation exchange and carbonate-bound adsorption for cadmium removal. The exchangeable fraction content in zeolite layers (7.91–12.70 mg/kg) was higher than in iron–carbon layers (2.88–5.98 mg/kg), indicating that zeolite possessed strong short-term adsorption capacity but presented risks of secondary release (Figure 4). From a spatial distribution perspective, the second layer served as the critical interface for cadmium migration and transformation. TF-CW's total cadmium accumulation (141.33 mg/kg) in Stage III was 18.09 mg/kg higher than FT-CW, suggesting that front-positioned iron–carbon layers (TF-CW) were more conducive to long-term immobilization through synergistic oxidation–adsorption mechanisms. The increase in cadmium accumulation from Stage II to III (such as FT-CW increasing from 105.28–123.24 mg/kg) may be related to adsorption saturation effects caused by substrate porosity (48.2–48.6%), with the pore structure influencing cadmium diffusion and retention. Speciation distribution analysis revealed that in the second layer, exchangeable (7.91–12.70 mg/kg) and carbonate-bound cadmium fractions in FT-CW during Stages II and III were significantly higher than in TF-CW (5.98–2.88 mg/kg), indicating that zeolite layers preferentially adsorbed cadmium through surface cation exchange and carbonate precipitation, while iron–carbon layers reduced cadmium bioavailability through redox reactions (Figure 4). Iron–carbon–zeolite composite substrates immobilized cadmium through dual redox–adsorption mechanisms; iron–carbon layers dominated mineral co-precipitation under oxidative conditions, while zeolite layers achieved short-term adsorption through ion exchange and carbonate binding. The TF-CW configuration (front-positioned iron–carbon) optimized the oxidation–adsorption sequence, making it more suitable for long-term cadmium contamination treatment and continuous remediation of high-cadmium-contaminated water bodies.

4. Conclusions

In this study, iron–carbon–zeolite CWs achieved efficient cadmium removal and system stability regulation through multidimensional mechanisms of "chemical immobilization–

plant enrichment–microbial metabolism", providing theoretical support for heavy metal-contaminated water remediation. The main conclusions are as follows:

(1) All systems achieved Cd^{2+} removal rates exceeding 99%, with iron–carbon substrate layers demonstrating significantly superior cadmium retention capacity. Zeolite layers exhibited higher NH_4^+-N removal efficiency through cation exchange.

(2) Under cadmium stress, *Typha* accumulated over 85% of the cadmium through root systems and regulated physiological metabolism, with dynamic responses closely associated with enhanced adaptability of the rhizosphere microbial communities. Iron–carbon substrates, due to the dominant role of iron/manganese oxide-bound fractions, demonstrated higher cadmium immobilization efficiency.

(3) Iron–carbon substrates significantly enhanced microbial diversity, promoting enrichment of functional bacterial phyla such as *Bacteroidota* and *Acidobacteriota*, as well as metal-tolerant genera, including *Saccharimonadales*, strengthening cadmium speciation transformation and stability through metabolic synergy.

Author Contributions: Conceptualization, M.L. and N.Z.; methodology, J.C.; validation, S.C.; formal analysis, J.C.; writing—original draft preparation, S.C.; formal analysis, J.C.; writing—review and editing, M.L., S.C., N.Z. and G.Y.; funding acquisition, G.Y. All authors have read and agreed to the published version of the manuscript.

Funding: This research was funded by the Hunan Provincial Natural Science Foundation of China (No. 2021JJ30728).

Data Availability Statement: Data is contained within the article.

Conflicts of Interest: Author Mengyi Li was employed by the company Anhui Hongsen High Technology Forestry Co., Ltd., Bozhou 236000, China. The remaining authors declare that the research was conducted in the absence of any commercial or financial relationships that could be construed as a potential conflict of interest.

References

1. Kotnala, S.; Tiwari, S.; Nayak, A.; Bhushan, B.; Chandra, S.; Medeiros, C.R.; Coutinho, H.D.M. Impact of heavy metal toxicity on the human health and environment. *Sci. Total Environ.* **2025**, *987*, 179785. [CrossRef]
2. Tan, Y.; Liu, X.; Shen, Z.; Xiao, Y.; Zhang, Y.; Du, H.; Wu, Z.; Zhi, D.; Núñez-Delgado, A.; Yang, Y. Effects of seed priming with different concentrations and forms of silicon on germination and growth of rice under cadmium stress. *Appl. Soil Ecol.* **2025**, *207*, 105947. [CrossRef]
3. Sasaki, T.; Horiguchi, H.; Matsukawa, T.; Kobayashi, M.; Omori, Y.; Oguma, E.; Komatsuda, A. A suspected case of "itai-itai disease" in a cadmium-polluted area in akita prefecture, Japan. *Environ. Health Prev. Med.* **2024**, *29*, 40. [CrossRef] [PubMed]
4. Yu, G.; Chen, H.; Chen, J.; Chen, S.; Long, Y.; Huang, J.; Wang, Y.; He, S. Enhanced nitrogen removal through aerobic denitrifying bacteria in horizontal subsurface flow constructed wetlands: Influencing factors and microbial community structure. *Chem. Eng. J.* **2024**, *481*, 148654. [CrossRef]
5. Wang, R.; Zhao, X.; Wang, T.; Guo, Z.; Hu, Z.; Zhang, J.; Wu, S.; Wu, H. Can we use mine waste as substrate in constructed wetlands to intensify nutrient removal? A critical assessment of key removal mechanisms and long-term environmental risks. *Water Res.* **2022**, *210*, 118009. [CrossRef]
6. Li, Y.; Zhang, M.; Wang, X.; Ai, S.; Meng, X.; Liu, Z.; Yang, F.; Cheng, K. Synergistic enhancement of cadmium immobilization and soil fertility through biochar and artificial humic acid-assisted microbial-induced calcium carbonate precipitation. *J. Hazard. Mater.* **2024**, *476*, 135140. [CrossRef]
7. Wang, X.; Wang, W.; Wang, W.; Dong, L.; Zhai, T.; Gao, Z.; Wang, K.; Wang, W.; Wang, S.; Kong, F. Enhanced effect and mechanism of nano fe-ca bimetallic oxide modified substrate on Cu(II) and Ni(II) removal in constructed wetland. *J. Hazard. Mater.* **2023**, *456*, 131689. [CrossRef]
8. Wang, G.; Yu, G.; Chi, T.; Li, Y.; Zhang, Y.; Wang, J.; Li, P.; Liu, J.; Yu, Z.; Wang, Q.; et al. Insights into the enhanced effect of biochar on cadmium removal in vertical flow constructed wetlands. *J. Hazard. Mater.* **2023**, *443*, 130148. [CrossRef]
9. Lichtenthaler, H.K.; Wellburn, A.R. Determinations of total carotenoids and chlorophylls a and b of leaf extracts in different solvents. *Biochem. Soc. Trans.* **1983**, *11*, 591–592. [CrossRef]

10. Loreto, F.; Velikova, V. Isoprene produced by leaves protects the photosynthetic apparatus against ozone damage, quenches ozone products, and reduces lipid peroxidation of cellular membranes. *Plant Physiol.* **2001**, *127*, 1781–1787. [CrossRef]
11. Heath, R.L.; Packer, L. Reprint of: Photoperoxidation in isolated chloroplasts I. Kinetics and stoichiometry of fatty acid peroxidation. *Arch. Biochem. Biophys.* **2022**, *726*, 109248. [CrossRef]
12. Stewart, R.R.C.; Bewley, J.D. Lipid peroxidation associated with accelerated aging of soybean axes. *Plant Physiol.* **1980**, *65*, 245–248. [CrossRef]
13. Bódog, I.; Polyák, K.; Csikós-Hartyányi, Z.; Hlavay, J. Sequential extraction procedure for the speciation of elements in fly ash samples. *Microchem. J.* **1996**, *54*, 320–330. [CrossRef]
14. Ventura, D.; Ferrante, M.; Copat, C.; Grasso, A.; Milani, M.; Sacco, A.; Licciardello, F.; Cirelli, G.L. Metal removal processes in a pilot hybrid constructed wetland for the treatment of semi-synthetic stormwater. *Sci. Total Environ.* **2021**, *754*, 142221. [CrossRef] [PubMed]
15. Faisal, A.A.H.; Taha, D.S.; Hassan, W.H.; Lakhera, S.K.; Ansar, S.; Pradhan, S. Subsurface flow constructed wetlands for treating of simulated cadmium ions-wastewater with presence of canna indica and typha domingensis. *Chemosphere* **2023**, *338*, 139469. [CrossRef] [PubMed]
16. Long, Y.; Yu, G.; Wang, J.; Zheng, D. Cadmium removal by constructed wetlands containing different substrates: Performance, microorganisms and mechanisms. *Bioresour. Technol.* **2024**, *413*, 131561. [CrossRef] [PubMed]
17. Zeng, Y.; Xu, L.; Su, J.; Liu, S.; Ali, A.; Zhang, P.; Cao, S. Denitrification driven by additional ferrous (Fe^{2+}) and manganous (Mn^{2+}) and removal mechanism of tetracycline and cadmium (Cd^{2+}) by biogenic Fe–Mn oxides. *Environ. Res.* **2024**, *246*, 118159. [CrossRef]
18. Wang, F.; Zeng, Y.-N.; Wang, Y.-T.; Li, J.-G.; Zhang, X.; Ji, A.-M.; Kang, L.-L.; Ji, R.; Yu, Q.; Gao, D.; et al. Highly efficient removal of hexavalent chromium by magnetic Fe-C composite from reed straw and electric furnace dust waste. *Environ. Sci. Pollut. Res.* **2023**, *30*, 33737–33755. [CrossRef]
19. Liu, M.; Wang, J.; Xu, M.; Tang, S.; Zhou, J.; Pan, W.; Ma, Q.; Wu, L. Nano zero-valent iron-induced changes in soil iron species and soil bacterial communities contribute to the fate of cd. *J. Hazard. Mater.* **2022**, *424*, 127343. [CrossRef]
20. Ben Salem, D.; Yahiaoui, K.; Bernardo, M.; Gatica, J.M.; Ouakouak, A.; Touahra, F.; Saad Eltaweil, A.; Tran, H.N. Insights into cadmium adsorption characteristics and mechanisms by new granular alginate hydrogels reinforced with biochar: Important role of cation exchange. *J. Environ. Manag.* **2025**, *383*, 125407. [CrossRef]
21. Li, Q.; Li, H.; Zong, X.; Sun, H.; Liu, Y.; Zhan, Z.; Mei, S.; Qi, Y.; Huang, Y.; Ye, Y.; et al. Highly efficient adsorption of ciprofloxacin from aqueous solutions by waste cation exchange resin-based activated carbons: Performance, mechanism, and theoretical calculation. *Sci. Total Environ.* **2024**, *912*, 169534. [CrossRef]
22. Si, T.; Yuan, R.; Qi, Y.; Zhang, Y.; Wang, Y.; Bian, R.; Liu, X.; Zhang, X.; Joseph, S.; Li, L.; et al. Enhancing soil redox dynamics: Comparative effects of Fe-modified biochar (N–Fe and S–Fe) on Fe oxide transformation and cd immobilization. *Environ. Pollut.* **2024**, *347*, 123636. [CrossRef]
23. Chen, Z.; Zheng, X.; Chen, Y.; Wang, X.; Zhang, L.; Chen, H. Nitrite accumulation stability evaluation for low-strength ammonium wastewater by adsorption and biological desorption of zeolite under different operational temperature. *Sci. Total Environ.* **2020**, *704*, 135260. [CrossRef]
24. Cao, J.; Li, N.; Jiang, J.; Xu, Y.; Zhang, B.; Luo, X.; Hu, Y. Activated carbon as an insoluble electron shuttle to enhance the anaerobic ammonium oxidation coupled with Fe(III) reduction process. *Environ. Res.* **2022**, *204*, 111972. [CrossRef]
25. Cisternas, J.; Rodríguez, C.; Serrano, J.; Leiva, E. Study of the key biotic and abiotic parameters influencing ammonium removal from wastewaters by Fe3+-mediated anaerobic ammonium oxidation (feammox). *Chemosphere* **2023**, *339*, 139463. [CrossRef]
26. Xiong, L.; Song, B.; Lin, X.; Wu, Y.; Yu, J.; Wang, X.; Huang, H.; Cheng, Y.; Zhou, Q.; Xue, G. Tuning pH to motivate chain reaction of iron release with extracellular polymeric substances formation for long lasting Fe0-driven autotrophic denitrification. *J. Environ. Manag.* **2025**, *384*, 125580. [CrossRef]
27. Yan, P.; Li, T.; Ren, T.; Zang, Y.; Sun, S.; Fan, Y.; Zhang, Y.; Gu, X.; He, S. Heterotrophic denitrification enhancement via effective organic matter degradation driven by suitable iron dosage in sediment. *J. Environ. Manag.* **2025**, *375*, 124275. [CrossRef] [PubMed]
28. Fu, X.; Hou, R.; Yang, P.; Qian, S.; Feng, Z.; Chen, Z.; Wang, F.; Yuan, R.; Chen, H.; Zhou, B. Application of external carbon source in heterotrophic denitrification of domestic sewage: A review. *Sci. Total Environ.* **2022**, *817*, 153061. [CrossRef] [PubMed]
29. Fu, Y.; Yang, X.; Shen, H. Root iron plaque alleviates cadmium toxicity to rice (*Oryza sativa*) seedlings. *Ecotoxicol. Environ. Saf.* **2018**, *161*, 534–541. [CrossRef] [PubMed]
30. Cui, Y.; Zhang, X.; Yang, P.; Liu, Y.; Song, M.; Su, G.; Guo, Y.; Yin, Y.; Jiao, W.; Cai, Y.; et al. Low-molecular weight organic acids can enhance the microbial reduction of iron oxide nanoparticles and pollutants by improving electrons transfer. *J. Hazard. Mater.* **2025**, *486*, 137123. [CrossRef]
31. Zhang, G.; Cui, J.; Song, J.; Ji, Y.; Zuo, Y.; Jia, H.; Yin, X. Transport of polystyrene nanoplastics with different functional groups in goethite-coated saturated porous media: Effects of low molecular weight organic acids and physicochemical properties. *J. Colloid Interface Sci.* **2024**, *653*, 423–433. [CrossRef]

32. Marchand, L.; Mench, M.; Jacob, D.L.; Otte, M.L. Metal and metalloid removal in constructed wetlands, with emphasis on the importance of plants and standardized measurements: A review. *Environ. Pollut.* **2010**, *158*, 3447–3461. [CrossRef] [PubMed]
33. Chen, C.; Yao, Y.; Xing, C.; Guo, Y.; Cai, L.; Yan, J.; Wu, X.-L.; Cai, M. Effects of zeolite imidazole frameworks on rice seedlings (*Oryza sativa* L.): Phytotoxicity, transformation, and bioaccumulation. *J. Environ. Sci.* **2024**, *144*, 15–25. [CrossRef] [PubMed]
34. Jia, L.; Liu, H.; Kong, Q.; Li, M.; Wu, S.; Wu, H. Interactions of high-rate nitrate reduction and heavy metal mitigation in iron-carbon-based constructed wetlands for purifying contaminated groundwater. *Water Res.* **2020**, *169*, 115285. [CrossRef] [PubMed]
35. Li, Y.B.; Song, J.L.; Yao, Q.J.; Chen, Z.X.; Wei, Y.; Li, H.L.; Wang, M.X.; Wang, B.J.; Zhou, J.M. Effects of dissolved oxygen on the sludge dewaterability and extracellular polymeric substances distribution by bioleaching. *Chemosphere* **2021**, *281*, 130906. [CrossRef]
36. Zhou, X.; Chen, Z.; Li, Z.; Wu, H. Impacts of aeration and biochar addition on extracellular polymeric substances and microbial communities in constructed wetlands for low C/N wastewater treatment: Implications for clogging. *Chem. Eng. J.* **2020**, *396*, 125349. [CrossRef]
37. Chen, Y.; Zhang, J.; Guo, Z.; Li, M.; Wu, H. Optimizing agricultural biomass application to enhance nitrogen removal in vertical flow constructed wetlands for treating low-carbon wastewater. *Environ. Res.* **2022**, *209*, 112867. [CrossRef]
38. Yu, L.; Hua, Z.; Liu, X.; Chen, L.; Zhang, Y.; Ma, Y.; Dong, Y.; Xue, H. The addition of iron-carbon enhances the removal of perfluoroalkyl acids (PFAAs) in constructed wetlands. *Environ. Pollut.* **2023**, *327*, 121534. [CrossRef]
39. He, Y.; Jiang, Z.; Zeng, M.; Cao, S.; Yu, X.; Wu, N. Deciphering retention effect of extracellular polymeric substances to typical heavy metals and their interaction with key inner enzymes of Candidatus Kuenenia. *J. Hazard. Mater.* **2024**, *477*, 135367. [CrossRef]
40. Shi, Y.; Huang, J.; Zeng, G.; Gu, Y.; Chen, Y.; Hu, Y.; Tang, B.; Zhou, J.; Yang, Y.; Shi, L. Exploiting extracellular polymeric substances (EPS) controlling strategies for performance enhancement of biological wastewater treatments: An overview. *Chemosphere* **2017**, *180*, 396–411. [CrossRef]
41. Ma, B.; Song, W.; Zhang, X.; Chen, M.; Li, J.; Yang, X.; Zhang, L. Potential application of novel cadmium-tolerant bacteria in bioremediation of cd-contaminated soil. *Ecotoxicol. Environ. Saf.* **2023**, *255*, 114766. [CrossRef]
42. Fierer, N.; Jackson, R.B. The Diversity and Biogeography of Soil Bacterial Communities. *Proc. Natl. Acad. Sci. USA* **2006**, *103*, 626–631. Available online: https://www.pnas.org/doi/epdf/10.1073/pnas.0507535103 (accessed on 5 July 2025).
43. Huang, X.; Yang, X.; Zhu, J.; Yu, J. Microbial interspecific interaction and nitrogen metabolism pathway for the treatment of municipal wastewater by iron carbon based constructed wetland. *Bioresour. Technol.* **2020**, *315*, 123814. [CrossRef]
44. Zhang, Z.; Li, D.; Liu, G.; Liu, T.; Feng, Y. Intensified nitrogen and phosphorus removal and mechanism revelation in constructed wetlands amended with iron-carbon based substrate towards low C/N ratio wastewater. *Chem. Eng. J.* **2024**, *481*, 148931. [CrossRef]
45. Pang, Q.; Xu, W.; He, F.; Peng, F.; Zhu, X.; Xu, B.; Yu, J.; Jiang, Z.; Wang, L. Functional genera for efficient nitrogen removal under low C/N ratio influent at low temperatures in a two-stage tidal flow constructed wetland. *Sci. Total Environ.* **2022**, *804*, 150142. [CrossRef] [PubMed]
46. Yin, S.; Yang, S.; Kou, X.; Sun, S. Removal Mechanisms of Single and Combined Pollutants of Cadmium and Antibiotics by Wetland Plants. *Asian J. Ecotoxicol.* **2024**, *19*, 127–149.

Disclaimer/Publisher's Note: The statements, opinions and data contained in all publications are solely those of the individual author(s) and contributor(s) and not of MDPI and/or the editor(s). MDPI and/or the editor(s) disclaim responsibility for any injury to people or property resulting from any ideas, methods, instructions or products referred to in the content.